A Comprehensive Quality Analysis of Empirical Green's Functions at Ocean-Bottom Seismometers in Cascadia

by Xiaotao Yang, Haiying Gao, Sampath Rathnayaka, and Cong Li

ABSTRACT

The deployment of oceanic seismic arrays facilitated unique data sets for the science community in imaging the seismic structures and understanding the lithosphere and mantle dynamics at subduction zone systems and other tectonic settings. The data quality is fundamental to ensure reliable seismic results using records from ocean-bottom seismometers. In this study, we conduct a comprehensive analysis of factors that may affect the signal-to-noise ratio (SNR) of the fundamental-mode Rayleigh waves, as a proxy for the waveform quality, within the Cascadia subduction zone. We use stations from Cascadia Initiative, Gorda deformation zone experiment, Blanco transform fault experiment, and Neptune Canada array. The empirical Green's functions (EGFs) of Rayleigh waves are extracted from ambient-noise seismic waveforms and filtered at 10- to 35-s periods. In general, the SNR of the EGFs decreases with increasing interstation distance and increasing sediment thickness. A portion of stations, mainly located within the Gorda plate and along the trench, demonstrates temporal variations of the data quality, with the highest SNR observed during the fall and winter seasons. The SNR demonstrates a complicated pattern in terms of the length of the time series used to extract EGFs. Most stations within the Juan de Fuca (JDF) plate show improvement of data quality with increasing length. However, for many stations located within the accretionary wedge and the Gorda plate, the ratio does not increase much by stacking more data. The distinctly different patterns of the SNR between the Gorda and JDF plates indicate possible impacts of lithosphere properties on data quality.

Electronic Supplement: Table showing the ocean-bottom seismometer (OBS) site parameters for selected examples analyzed in the main article and figures providing channel information, examples of empirical Green's functions (EGFs), and distribution of average signal-to-noise ratios of the EGFs for all OBS in Cascadia.

INTRODUCTION

The deployment of seismic arrays on ocean floor, that is, ocean-bottom seismometers (OBSs), facilitated unique data sets for studying the structures of oceanic lithosphere and upper mantle. Many studies used data from OBS deployments at different tectonic environments such as the East Pacific Rise (e.g., Forsyth *et al.*, 1998; Hammond and Toomey, 2003), the Cascadia region (e.g., Bodmer *et al.*, 2015; Gao and Shen, 2015; Gao, 2016, 2018; Byrnes *et al.*, 2017; Eilon and Abers, 2017; Rathnayaka and Gao, 2017; VanderBeek and Toomey, 2017), the eastern North America margin (e.g., Lynner and Porritt, 2017), the Lau basin (e.g., Zha *et al.*, 2014; Wei *et al.*, 2015; Zha and Webb, 2016), and the Mid-Atlantic Ridge (e.g., Collins *et al.*, 2012; Paulatto *et al.*, 2015; Eason *et al.*, 2016). Results from these studies have significantly contributed to our understanding of dynamics within the interior of the Earth, especially on the ocean side. Among a variety of seismic methods used, ambient-noise tomography has been popularly applied to image the crust and mantle lithosphere structure (e.g., Shapiro *et al.*, 2005; Harmon *et al.*, 2007; Lin *et al.*, 2008; Yao *et al.*, 2011; Tian *et al.*, 2013; Shen and Ritzwoller, 2016; Rathnayaka and Gao, 2017; Gao, 2018).

To implement seismic ambient-noise tomography, one fundamental step is to extract high-quality surface-wave empirical Green's functions (EGFs) through the cross correlation of continuous seismic waveforms between station pairs (e.g., Shapiro *et al.*, 2005; Bensen *et al.*, 2007; Zhang, 2010). The primary sources of ambient noise are oceanic microseisms (e.g., Yang and Ritzwoller, 2008; Tian and Ritzwoller, 2015). For continental stations, EGFs can be retrieved at a wide range of periods up to a few hundred seconds (Bensen *et al.*, 2007; Gao and Shen, 2014; Savage *et al.*, 2017). However, for OBS stations, the seismic energies are contaminated by low-frequency oceanic infragravity waves (Webb, 1998; Tian and Ritzwoller, 2017), and the peak microseisms are recorded at periods less than 33 s (Webb, 1998). Furthermore, oceanic microseisms mainly originate from winter storms in the northern hemisphere and summer storms in the southern hemisphere (Webb, 1998). The seasonality of oceanic microseisms may result in temporal variations of the EGFs at OBS stations.

In addition to far-field ambient noises, OBS instruments are vulnerable to local noises associated with site conditions

doi: 10.1785/0220180273

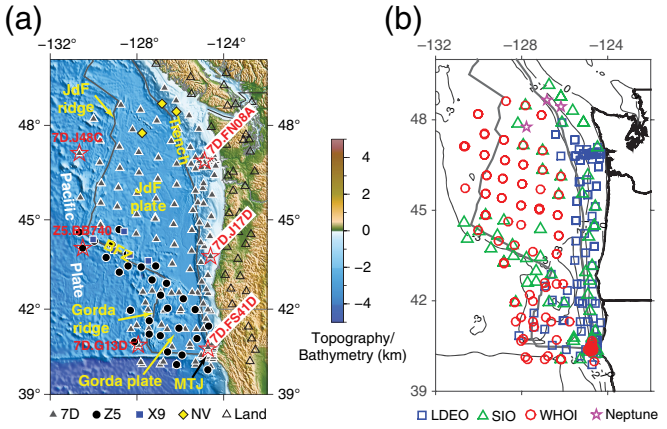

▲ **Figure 1.** Distribution of the seismic stations in Cascadia used in this study. (a) 7D, Cascadia Initiative; Z5, Gorda deformation zone experiment; X9, Blanco transform fault experiment; NV, Neptune Canada array. Open triangles are inland stations from miscellaneous networks. Stations enclosed by stars are shown in Figures 4–7. Station names are labeled following the format of net-code.site-name. JdF, Juan de Fuca; BFZ, Blanco fracture zone; MTJ, Mendocino triple junction. (b) Stations grouped by ocean-bottom seismometer (OBS) host institutions. LDEO (squares), Lamont–Doherty Earth Observatory; SIO (triangles), Scripps Institution of Oceanography; WHOI (circles), Woods Hole Oceanographic Institution; Neptune (stars), the Neptune Canada array. The color version of this figure is available only in the electronic edition.

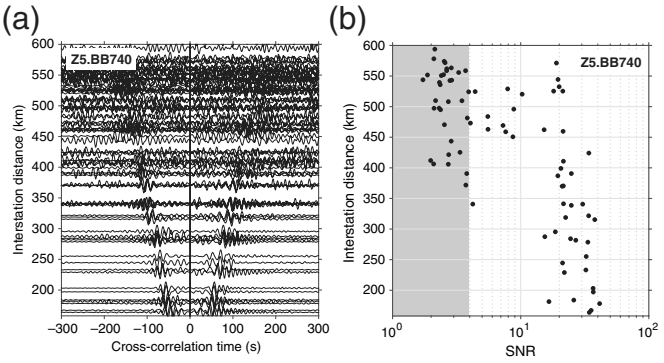

▲ **Figure 2.** Examples of empirical Green's functions (EGFs). (a) Waveforms from the virtual source Z5.BB740 to other stations. (b) The signal-to-noise ratios (SNRs) corresponding to the EGFs in (a). The EGFs are filtered at 10–35 s. See the station location in Figure 1a. The shaded area in (b) highlights the range of SNRs below 4, within which no clear surface waves can be identified from the EGFs.

such as water depth and sediment thickness (Webb, 1998; Bell *et al.*, 2015; Sumy *et al.*, 2015; Tian and Ritzwoller, 2017; Gomberg, 2018). For example, the seismic recordings at shallow-water instruments can be easily perturbed by the interaction of ocean currents with the sea floor. Sumy *et al.* (2015) observed very high noise power of raw waveforms at Cascadia Initiative OBS stations in shallow-water regions, which was attributed to the effect of wind and wave interactions. The EGFs at those shallow-water stations also appear to be very noisy (Tian and Ritzwoller, 2017). The thick marine sediments can significantly affect the site response of OBS stations and prolong the surface-wave durations (Gomberg, 2018).

In this study, we conduct a systematic and quantitative analysis of the signal-to-noise ratio (SNR) of the fundamental-mode Rayleigh waves within the Juan de Fuca (JdF) and Gorda plates of the Cascadia subduction zone. Our goal is to analyze the influence of seasonal variations and site conditions on the quality of surface-wave EGFs. The OBS deployments in Cascadia spanned over a period of 4 yrs in multiple phases and covered the entire subduction system, providing excellent data sets for our analysis. Our results show that the SNR of EGFs decreases with increasing interstation distance, decreasing water depth, and increasing sediment thickness. These are the general trends that have been commonly observed (Webb, 1998; Bell *et al.*, 2015; Sumy *et al.*, 2015; Tian and Ritzwoller, 2017; Gomberg, 2018). A new finding from our analysis is that a portion of OBS sites demonstrate very strong seasonal variations, most of which are located within the Gorda plate. In addition, we observe remarkable differences in the data quality between stations within the JdF plate and those within the Gorda plate. Our analysis provides beneficial information in guiding data selections for seismic ambient-noise tomography and in optimizing the performance of future OBS deployments.

DATA AND METHOD

Empirical Green's Functions

Rayleigh-wave EGFs can be extracted from the cross correlation of vertical-component continuous waveforms between two stations (Shapiro *et al.*, 2005; Bensen *et al.*, 2007). We used the EGF data set from Gao (2016, 2018), retrieved from seismic waveforms between 2011 and 2015 from 266 oceanic stations and 35 continental stations (see station distribution in Fig. 1a). Gao and Shen (2014) fully described the procedures to extract EGFs that we used for data quality analysis in this study. Specifically, before cross-correlation of the vertical-component waveforms between each station pair, the instrument response was removed, followed by a frequency–time normalization method (Shen *et al.*, 2012) to normalize the ambient-noise data. The frequency–time normalization method improves the SNR of EGFs by a factor of ~2 in comparison with the one-bit normalization method (Shen *et al.*, 2012). The time segments of large (magnitude > 5.5) earthquakes were eliminated, and the daily cross-correlations were stacked for each station pair. The EGFs were computed as the negative time derivatives of the stacked cross-correlations (Shen *et al.*, 2012). The analyzed EGFs between station pairs are 1000 s long, with one sample per second, for both positive and negative segments. To identify appropriate periods for the analysis, we filtered the OBS EGFs at multiple narrow period bands, ranging from 10 to 15 s, 15 to 20 s, 20 to 25 s, 25 to 30 s, 30 to 35 s, and 35 to 40 s. Examples of the EGFs in Figure 2 and Ⓔ Figure S2 (available in the electronic supplement to this article) show clear

surface-wave signals at the periods between 10 and 35 s, with dominant periods at 10–25 s. Hereafter, we use the filtered EGFs at periods of 10–35 s (i.e., a central period of 22.5 s), which is the period range of typical oceanic microseisms (Webb, 1998), for data quality analysis.

A common practice to improve the EGF data quality is by stacking the daily data over the duration of the time series (e.g., Bensen *et al.*, 2007). In this study, to examine temporal variations of EGFs, we include two types of data sets: (1) EGFs from the stack of every 30 consecutive days, referred to as single monthly stack, and (2) EGFs from the accumulative stack of single monthly stacks, referred to as accumulative monthly stack. As shown in Ⓔ Figure S3, the durations of the cross-correlated data between most OBS station pairs are about 6–10 months but are up to 4 yrs for some long-running continental station pairs.

We use SNR to quantify the quality of the fundamental-mode Rayleigh-wave EGFs between station pairs. Here, the SNR is defined as the ratio of the maximum signal amplitude to the root mean square of the noise amplitude. The starting time of the signal is defined using a Rayleigh-wave velocity of 4.5 km/s, and the signal length is set as three times of the longest period. The noise window starts 105 s, which is three times of the longest period, after the signal window and has the same length as the signal. To minimize the asymmetric effect of EGFs, we first calculated separately the SNRs for the positive and negative segments and then took the average as our SNR between the station pair. The Rayleigh-wave signals can be clearly identified in EGFs with SNR greater than 4 (Fig. 2). We thus use SNR of 4 as a threshold to classify the EGFs into noisy (SNR ≤ 4) and good (SNR > 4).

Instrumentation of the Seismic Stations

The OBSs analyzed in this study are from four seismic experiments, including the Cascadia Initiative Amphibious array (see Data and Resources), the Gorda deformation zone experiment (see Data and Resources), the Blanco transform fault experiment (see Data and Resources), and the Neptune Canada experiment (Barnes *et al.*, 2008). The Cascadia Initiative was deployed in four phases during 2011–2015, covering the entire JdF and Gorda plates (Toomey *et al.*, 2014). The OBS instruments were provided by Lamont–Doherty Earth Observatory (LDEO), Scripps Institution of Oceanography (SIO), and Woods Hole Oceanographic Institution (WHOI; Fig. 1b). The Gorda experiment spanned across the Blanco fracture zone and the entire Gorda plate from 2013 to 2015, operated by LDEO and SIO. The Blanco experiment covered the entire Blanco transform fault during 2012–2013, operated by WHOI. The long-term Neptune Canada experiment is a cabled OBS array deployed in the northernmost JdF plate since 2009.

Within the Cascadia subduction system, the water depth varies from > 4000 m at the JdF and Gorda spreading centers to about 2000 m along the deformation front and less than 100 m immediately off the coastal margin. The bathymetric gradient within the Gorda plate is much sharper than that within the JdF plate (Fig. 1a). The Neptune Canada stations are located at water depths of 400–2500 m (stars in Fig. 1b). All the WHOI

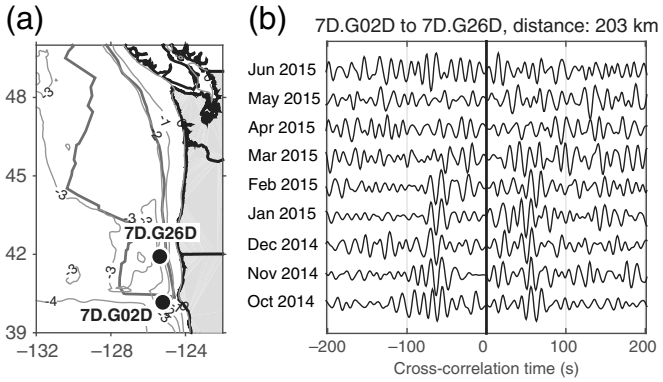

▲ **Figure 3.** Examples of single monthly stacked EGFs illustrating the temporal variation of EGFs between the station pair of 7D.G02D and 7D.G26D. (a) Station locations (dots). (b) Positive time lag means ambient noises propagating northward from 7D.G02D to 7D.G26D. Negative time lag means ambient noises propagating southward from 7D.G26D to 7D.G02D.

stations were deployed at water depths greater than 2000 m, covering the Gorda and JdF plates (circles in Fig. 1b). The LDEO stations were located along the accretionary wedge and within the Gorda plate (squares in Fig. 1b). Some of LDEO stations at shallow water depths (< 1000 m) were equipped with trawl-resistant shields to protect against instrument damage caused by trawl fishing and to potentially reduce noise from ocean currents (Sumy *et al.*, 2015). The SIO stations cover a broad range of water depths (triangles in Fig. 1b).

Four vertical channels—BHZ, HHZ, EHZ, and ELZ—are used by the OBS stations in this study. The EHZ and ELZ channels are designed to record high-frequency (> 1 Hz) seismic signals, which are far beyond the frequency range of the oceanic microseisms (Webb, 1998). Therefore, we only considered BHZ and HHZ channels, which are generally sensitive to a broad frequency band ranging from 0.01 to 10 Hz. The SIO and WHOI OBSs provide both BHZ and HHZ channels, and the LDEO and Neptune Canada stations only have HHZ channels (see Ⓔ Fig. S1).

In addition, we chose 35 continental seismic stations with BHZ channels to provide a first-order comparison of data quality with OBSs, although this is not the focus of this study. The continental stations are selected from the EarthScope Transportable Array (see Data and Resources), the Pacific Northwest Seismic Network (see Data and Resources), the Canadian National Seismograph Network (see Data and Resources), the University of Oregon Regional Network, the Global Seismograph Network (see Data and Resources), and the United States National Seismic Network (see Data and Resources).

RESULTS

In this section, we provide a comprehensive analysis of the data quality of the EGFs in terms of seasonality (Figs. 3–5) and site

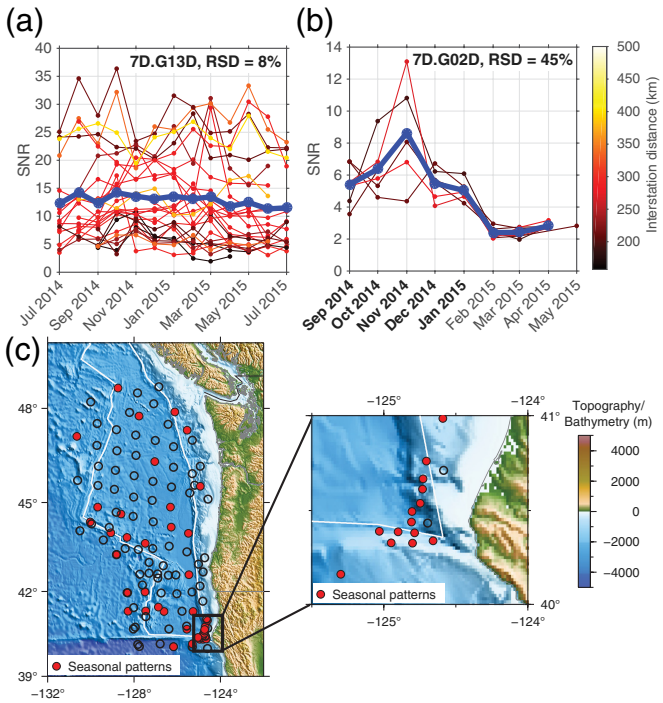

▲ **Figure 4.** Temporal variations of the SNR of single monthly stacked EGFs. (a) An example of OBS stations without clear seasonal patterns (see Fig. 1 for station location). (b) An example showing strong seasonal variation of EGFs observed in this study (see Fig. 3 for station location). The horizontal axis in (a,b) is the calendar month corresponding to the middle of the 30-day period for each stack. The data are color-coded by interstation distance. The thick lines in (a,b) are the average SNRs of the single monthly stacks among all the station pairs from the same virtual sources. The relative standard deviation (RSD) is computed as the standard deviation normalized by the mean of the average monthly SNRs, scaled to 0%–100%. (c) Distribution of the OBS stations showing seasonal variations of EGFs (filled circles). The color version of this figure is available only in the electronic edition.

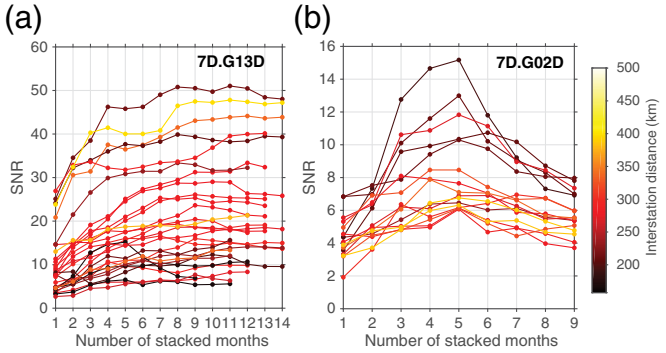

▲ **Figure 5.** Variations of the SNR with the time-series length used to stack EGFs at stations (a) 7D.G13D and (b) 7D.G02D. The horizontal axis is the number of nominal months, which are 30-day periods, used in producing the stacked EGFs. Each line of connected dots represents the measurement for one station pair. The data are color-coded by interstation distance. See the station locations in Figure 1. The color version of this figure is available only in the electronic edition.

conditions (Figs. 6–9), which include water depth, sediment thickness, tectonic unit, and geographic location.

Seasonality of EGFs

We noticed that the SNRs of EGFs between some OBS station pairs demonstrate temporal variations to a certain extent (Fig. 3). To explore the seasonal variations of EGFs, we require (1) a minimum of three receivers from each virtual source with interstation distance less than 400 km; (2) at least 7-month data recordings; and (3) the average SNR of all single monthly stacks is greater than 4. With these criteria, we excluded 130 OBS stations for further analysis, most of which are located within the accretionary wedge at relatively shallow water (Ⓔ Fig. S4). For dropped stations at deep water within the JdF plate (Ⓔ Fig. S4), most of them were excluded because of insufficient data length. To be classified as a station with seasonal variations, the SNR distributions among at least three station pairs must show distinct and consistent temporal dependence. Furthermore, we calculated the average SNR of single monthly stacks among all the station pairs from the same virtual source to quantify the seasonality of EGFs (thick lines in Fig. 4a,b). The relative standard deviation is defined as the standard deviation normalized by the mean of the averaged monthly SNRs, scaled to 0%–100%. For example, the average monthly SNR from the virtual source 7D.G02D reaches its maximum (up to 9) in the fall and winter seasons and decreases to below 4 beginning in February 2015 (Fig. 4b). The relative standard deviation of the average monthly SNR is about 45%, demonstrating a strong seasonal variation of the data quality. In contrast, the average monthly SNR from 7D.G13D varies within a narrow range of 10–15 with a small relative standard deviation (8%), showing no seasonal dependence. Among the 136 OBS stations examined, there are 47 stations showing clear seasonal variations (filled circles in Fig. 4c), which are dominantly located at the Mendocino triple junction, along the trench and the Gorda ridge, and near the Blanco fracture zone.

In overall, the SNRs of accumulative monthly stacks of EGFs increase with the number of months used to extract EGFs (Fig. 5a), which satisfies the power-law relationship (Bensen *et al.*, 2007). This observation is applicable to most of the Cascadia OBS stations with weak or no seasonal variations of EGFs. Approximately after 6-month data stacking, the SNRs become relatively stable. However, at stations with strong seasonal variations, the SNRs of accumulative monthly stacks first show a dramatic increase toward the peak-SNR seasons and then decrease gradually afterward (Fig. 5b).

Distribution of SNRs in Terms of Site Conditions

To separate the impact of data length on the quality of EGFs, here we focus our analysis on the SNRs of the stacked EGFs using 6 months' data (Figs. 6 and 7). We also computed the average SNR of the EGFs from each station to all the receivers to examine the average distribution pattern of the data quality

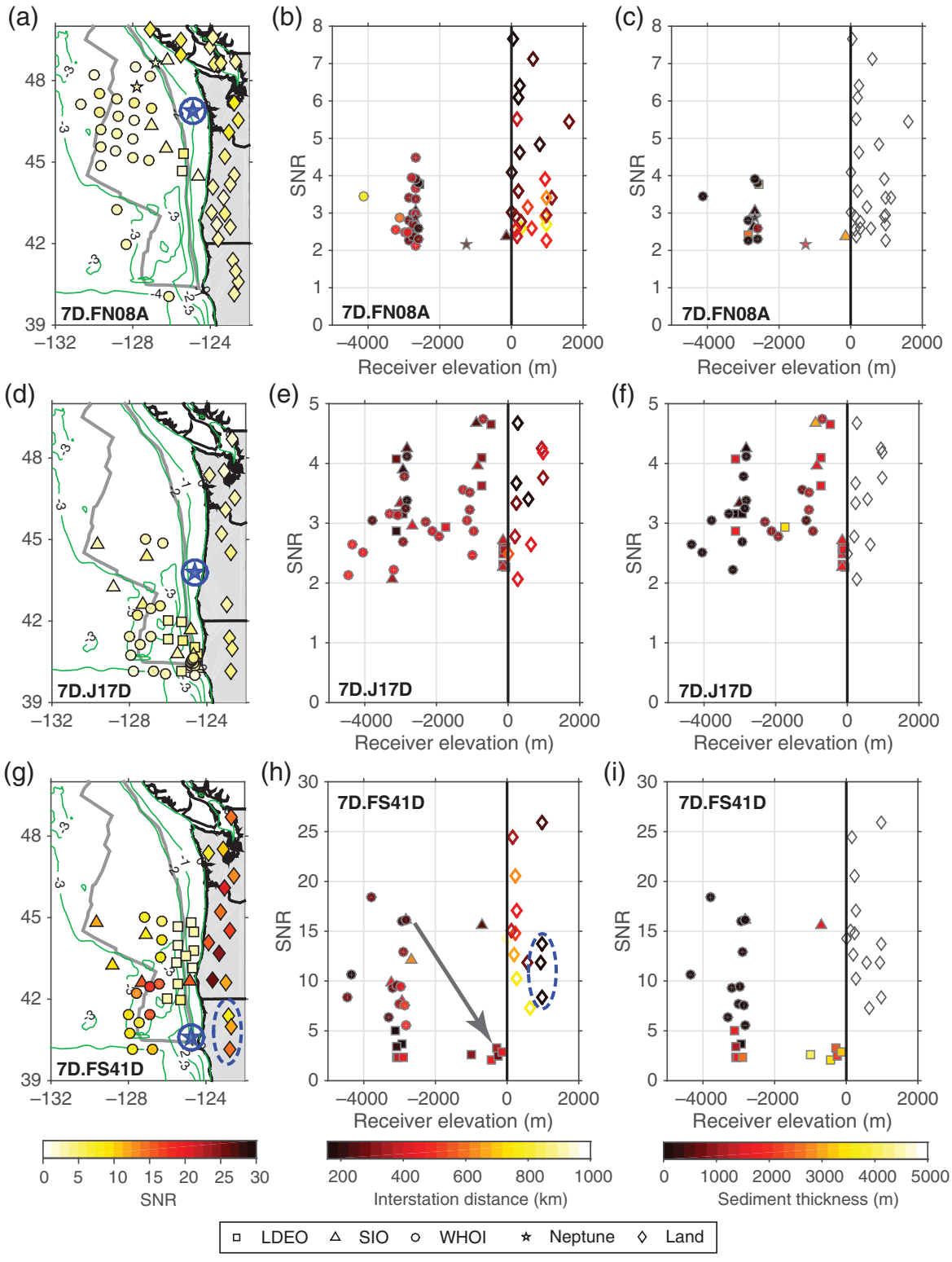

▲ **Figure 6.** Distribution of the SNR of stacked EGFs using 6 months' data from shallow-water virtual sources (a–c) 7D.FN08A, (d–f) 7D.J17D, and (g–i) 7D.FS41D. (a,d,g) The location of the virtual source (circled star) and the receivers (filled symbols), color-coded by the SNR values. The contour lines show the bathymetry from ETOPO1. (b,e,h) The SNR distribution in terms of the receiver elevation (water depth for OBS), grouped by institutions and color-coded by interstation distance. (c,f,i) The same data as (b,e,h) but are color-coded by the sediment thickness from Gomberg (2018). Stations operated by different institutions are plotted as different symbols (see legend at the bottom). The arrow in (h) highlights the decrease of SNRs toward shallow-water receivers. The dashed ellipse in (h) corresponds to the group of stations in northern California in (g). The color version of this figure is available only in the electronic edition.

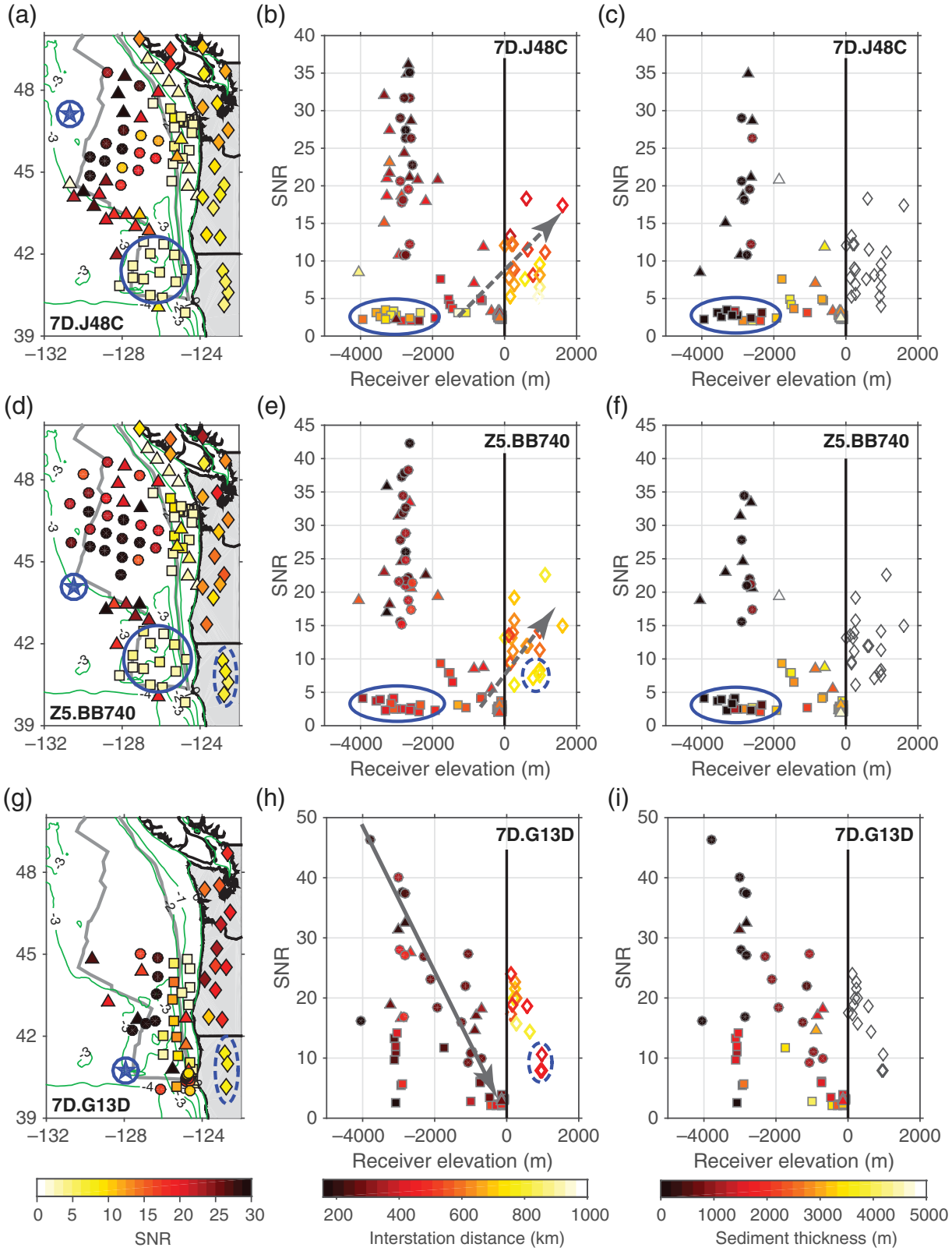

▲ **Figure 7.** Distribution of the SNR of stacked EGFs using 6 months' data from deep-water virtual sources (a–c) 7D.J48C, (d–f) Z5.BB740, and (g–i) 7D.G13D. The arrows in (b,h) highlight the change of SNRs from OBS to land stations and from deep water to shallow water, respectively. The ellipses in (b,c) and (e,f) correspond to the outlined stations within the Gorda plate in (a) and (d), respectively. The dashed ellipses in (e,h) correspond to the group of stations in northern California in (d,g). The color version of this figure is available only in the electronic edition.

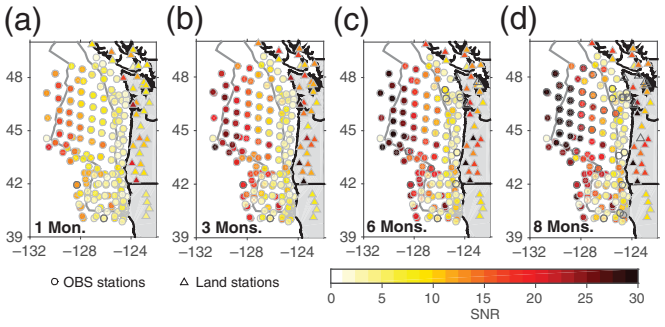

▲ **Figure 8.** Distribution of the average SNR of EGFs at the period of 10–35 s at OBSs (dots) and land stations (triangles). The EGFs are stacked at data length of (a) 1 month, (b) 3 months, (c) 6 months, and (d) 8 months. Stations without enough data for the corresponding time-series length are plotted as open symbols in each subplot. See Ⓔ Figure S5 (available in the electronic supplement to this article) for the distribution of SNR for EGFs stacked using data length of 1–12 months, in which the stations are grouped by OBS institutions. The color version of this figure is available only in the electronic edition.

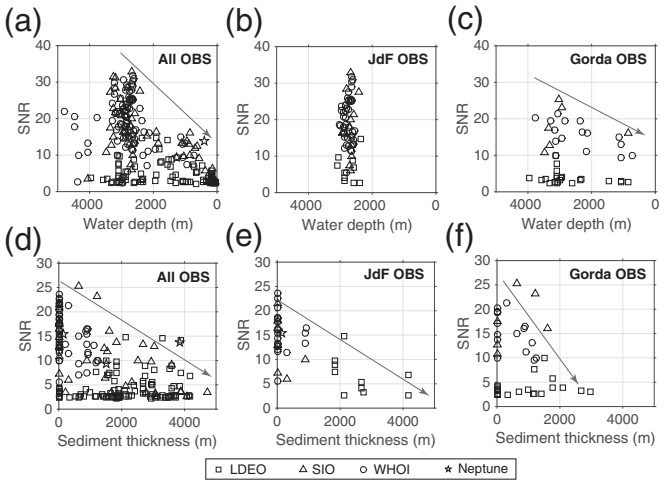

▲ **Figure 9.** Distribution of the average SNR with (a–c) water depth and (d–f) sediment thickness. The EGFs are stacked using 6 months' data. (a,d) The SNR distribution for all OBS stations. (b,e) The SNR distribution for OBS stations located between the JdF ridge and the trench. (c,f) The SNR distribution for OBS stations located between the Gorda ridge and the trench. The arrows mark the general trends of decreasing SNRs with decreasing water depth and increasing sediment thickness. The sediment thickness data in (d–f) are referred from Gomberg (2018).

(Figs. 8 and 9). Considering the generally decreasing of SNRs with interstation distance (Fig. 2), we require a source-to-receiver distance of 158–236 km, which is 1–1.5 times of the maximum wavelength using a surface-wave velocity of 4.5 km/s for our longest period of 35 s.

In general, the SNRs from shallow-water virtual sources appear to be much lower (< 10, Fig. 6a–f) compared with the ratios at deep-water virtual sources (up to 50, Fig. 7), regardless of the receiver locations. Figure 6a,d shows the representative distributions of the EGF SNRs from shallow-water virtual sources (< 500 m) to receivers located from the spreading centers to onshore, which are characterized by a cluster of very low SNRs below 7. One exception is the EGFs from station 7D.FS41D (water depth of 1079.3 m, see Ⓔ Table S1) located near the Mendocino triple junction, which have much higher SNRs (up to 20, Fig. 6g).

For virtual sources located at deep water, we observed very complicated SNR patterns (Fig. 7). First, the SNRs decrease from deep-water receivers (≤ 45) to shallow-water receivers (< 4) and then increase at the continental stations (≤ 25). Second, from the same virtual source, the SNRs appear to be higher at receivers within the JdF plate than those within the Gorda plate (Fig. 7a, d). Third, the SNRs decrease with increasing interstation distance from the same virtual source to receivers at similar water depths (Fig. 7b,e).

The distribution pattern of average SNRs at each station demonstrates the difference of data quality between the JdF and Gorda plates (Figs. 8 and 9, and Ⓔ Fig. S5). In Figure 9, we plot the distribution of EGF SNRs for OBS stations within the JdF plate (between the JdF ridge and the trench) and the Gorda plate (between the Gorda ridge and the trench), separately. Within the JdF plate, the average SNRs decrease gradually away from the JdF ridge and increase with increasing data length (Fig. 8). For example, with 6 months' data (Figs. 8c and 9b), the SNRs vary from > 30 to < 5 within the JdF plate within a relatively narrow bathymetry range. In contrast, the SNRs at stations within the Gorda plate range from about 25 to < 5 and overall are lower than those within the JdF plate (Figs. 8 and 9b,c). Within the Gorda plate, the SNRs are generally decreasing with the decrease of water depth (Fig. 9c). In addition, the LDEO OBSs within the Gorda plate have relatively lower SNRs at the period we use compared with other OBSs (Figs. 7a,d and 9c,f) and demonstrate no clear dependence on data length (Ⓔ Fig. S5). At the accretionary wedge between the trench and the coastline, the average SNRs at most OBS stations are lower than 5, regardless of the number of months used to extract the EGFs (Fig. 8).

Our results show that the SNR decreases with increasing sediment thickness (Figs. 7c,f,i and 9d–f). This pattern is clearly shown for oceanic stations within the JdF plate (Fig. 9e), where the water depth varies at 2400–3000 m between the trench and the ridge (Fig. 9b). A similar SNR pattern is also observed at stations within the Gorda plate, with sediments 0–2000 m thick (Fig. 9f). Here, we refer to the study by Gomberg (2018) for the sediment thickness at each station, defined as the depth to the 4.5 km/s *P*-wave velocity isosurface. The EGF SNRs are lower than 10 at most of the OBS sites with sediment thicknesses > 2500 m (Figs. 6i and 7c,f,i). In addition, we observe distinct along-strike variations of the SNR for the continental stations (Fig. 8). Stations located in northernmost California have lower SNRs (< 10) than those in western Oregon and western Washington (≤ 30). This pattern is clearly shown in both the average SNRs (Fig. 8) and the SNRs for individual station pairs (Figs. 6g, and 7d,g).

DISCUSSION

The seasonal variations of seismic ambient noises have been widely observed at both oceanic and continental stations. At the Pacific Northwest, the dominant source of ambient noises originates from the interaction of the Pacific Ocean with the coastlines and the seafloor (Schulte-Pelkum *et al.*, 2004; Yang and Ritzwoller, 2008). For continental station pairs at 5- to 20-s periods, Yang and Ritzwoller (2008) documented higher quality EGFs during the winter season compared with the summer season in the northern hemisphere. There is much less seasonal variations at periods > 20 s (Yang and Ritzwoller, 2008). Tian and Ritzwoller (2015) observed azimuth-dependent seasonal variations of EGFs for Cascadia Initiative OBS stations located within the central and northern JdF plate. In this study, we analyzed the distribution pattern of Rayleigh-wave EGFs in the entire Cascadia subduction system from multiple OBS deployments over a 4-yr period (Fig. 1a).

A majority of OBS stations located within the accretionary wedge, where the sediment is about 4–6 km thick, recorded very noisy EGFs. The decrease of the EGF SNRs with increasing sediment thickness may be explained by the contamination from the resonance of seismic waves at different frequencies trapped within the sedimentary layer. Gomberg (2018) showed that within thick sediments (> 2000 m), the resonant frequencies are generally below 0.2 Hz, corresponding to periods longer than 5 s. At stations in very shallow water region, the interaction of oceanic waves with the coastlines may disturb the instruments, generating local noises that may contaminate the seismic recordings. Furthermore, the water flow within submarine canyons and turbidites caused by underwater landslides at the continental slope (Goldfinger *et al.*, 2000, 2017) may introduce additional local noises. The quality of OBS recordings at periods longer than 10 s at shallow-water environment can be improved through tilt and compliance corrections (Crawford and Webb, 2000; Bell *et al.*, 2015; Tian and Ritzwoller, 2017), although the pattern of decreasing SNRs toward shallow water remains true, as shown by Tian and Ritzwoller (2017). Additionally, some closely deployed stations demonstrate very different EGF SNR patterns (Figs. 4c and 8), which may reflect differences in local bathymetry, operational season of the year, and instrumentation. However, it is extremely difficult to isolate the impact of these factors on the SNRs.

Our results document distinct differences in the quality of EGFs between the JdF and Gorda plates in terms of seasonality, site conditions, and data length. Many stations within the Gorda plate show strong seasonal variations of EGFs, with the highest SNRs during the fall and winter seasons. Most of these stations are located at places with relatively sharp bathymetric gradients (Fig. 4e), such as the Gorda ridge and the Mendocino triple junction (Dziak *et al.*, 2001). In contrast, no clear seasonal patterns are observed at most stations within the interior of the JdF plate. The contrasting EGF seasonality between the Gorda and JdF plates suggests that bathymetric gradient may be one key factor that affects the propagation of oceanic microseisms along the seafloor. The seasonality of EGFs at OBS stations has significant implications for ambient-noise tomographic studies as well as future marine seismic deployments. To optimize the performance of OBS stations, we suggest that the deployment should cover at least the fall and winter months in the northern hemisphere. To maximize the surface-wave signals, it would be optimal to stack the EGFs within the peak seasons instead of through the total duration of the time series, particularly for stations showing strong seasonal variations of EGFs.

The overall quality of EGFs at stations within the Gorda plate is also distinctly lower compared with stations within the JdF plate (Figs. 4, 8, and 9). The different distribution patterns of the SNRs between these two plates may partly reflect the fundamental differences in the crust and mantle lithosphere properties. The Gorda plate is relatively younger than the JdF plate from seafloor ages (Müller *et al.*, 2008). In addition, the Gorda plate is characterized by widely distributed internal deformations (Wilson, 1989; Dziak *et al.*, 2001), which are associated with abundant intraslab earthquakes (Smith *et al.*, 1993; Velasco *et al.*, 1994; Bakun, 2000; Wong, 2005). As examined by Bensen *et al.* (2007), earthquake signals, if not eliminated, appear as spurious precursory arrivals on the EGFs, which may contribute to the low SNRs observed within the Gorda plate. In addition, seismic studies have shown prominently low shear-wave velocities and high attenuations within the Gorda oceanic lithosphere, which suggest the presence of partial melt and/or a relatively warm and weak lithosphere (Byrnes *et al.*, 2017; Eilon and Abers, 2017). Consequently, the propagation of Rayleigh waves within the Gorda plate may decay faster than those within the JdF plate.

CONCLUSIONS

In this study, we investigated possible factors that may affect the quality of ambient-noise waveforms within the entire Cascadia subduction system. On average, the SNR of the Rayleigh-wave EGFs decreases with increasing interstation distance and increasing sediment thickness. We observed seasonal variations of the EGFs at 47 OBS stations, most of which are located at the Mendocino triple junction, along the trench and the Gorda ridge, and near the Blanco fracture zone, with the peak seismic energy in fall and winter months. Our analysis demonstrated that at stations showing seasonally varied EGFs, the data quality of the stacked EGFs may decrease, instead of increase, with the increasing length of the time series. Within the JdF plate, the SNR decreases gradually from ridge to trench, with the lowest ratios observed within the accretionary wedge. In contrast, within the Gorda plate, the ratios are on average very low and demonstrate strong variations among stations. The distribution patterns of the data quality reflect the fundamental differences between the Gorda and JdF plates in the bathymetric gradient, the seismicity rate, and the crust and mantle lithosphere structures.

DATA AND RESOURCES

The ETOPO1 topography data set used in this study was downloaded from National Centers for Environmental Information

(https://www.ngdc.noaa.gov/mgg/global/global.html, last accessed September 2018). The ocean-bottom seismometer (OBS) instrument information in Ⓔ Table S1, available in the electronic supplement to this article, was downloaded from Incorporated Research Institutions for Seismology (IRIS) Data Management Center (DMC) MetaData Aggregator (http://ds.iris.edu/mda, last accessed September 2018). Figures 1a and 4c in this study were produced using the Generic Mapping Tools (GMT) v.4.5.7 (http://gmt.soest.hawaii.edu, last accessed September 2018). The other data are from the following sources: Cascadia Initiative Amphibious array (doi: 10.7914/SN/7D_2011), the Gorda deformation zone experiment (doi: 10.7914/SN/Z5_2013), the Blanco transform fault experiment (doi: 10.7914/SN/X9_2012), EarthScope Transportable Array (doi: 10.7914/SN/TA), the Pacific Northwest Seismic Network (doi: 10.7914/SN/UW), the Canadian National Seismograph Network (doi: 10.7914/SN/CN), the Global Seismograph Network (doi: 10.7914/SN/IU), and the United States National Seismic Network (doi: 10.7914/SN/US).

ACKNOWLEDGMENTS

The authors thank Associate Editor Brandon Schmandt and two anonymous reviewers for their constructive comments. The authors are grateful to Spahr Webb for valuable discussions on the signal-to-noise ratio patterns presented in this study. All ocean-bottom seismometer data used in this research were provided through Incorporated Research Institutions for Seismology Data Management Center by instruments from the Ocean Bottom Seismograph Instrument Pool (OBSIP). OBSIP is funded by the National Science Foundation. This research was supported by the National Science Foundation (Grant Number EAR-1624077) and the startup funding for Haiying Gao at the University of Massachusetts Amherst.

REFERENCES

Bakun, W. H. (2000). Seismicity of California's north coast, *Bull. Seismol. Soc. Am.* **90,** 797–812.

Barnes, C. R., M. M. R. Best, and A. Zielinski (2008). The NEPTUNE Canada regional cabled ocean observatory, *Sea Technol.* **49,** 10–14.

Bell, S. W., D. W. Forsyth, and Y. Ruan (2015). Removing noise from the vertical component records of ocean-bottom seismometers: Results from year one of the Cascadia Initiative, *Bull. Seismol. Soc. Am.* **105,** 300–313.

Bensen, G. D., M. H. Ritzwoller, M. P. Barmin, A. L. Levshin, F. Lin, M. P. Moschetti, N. M. Shapiro, and Y. Yang (2007). Processing seismic ambient noise data to obtain reliable broad-band surface wave dispersion measurements, *Geophys. J. Int.* **169,** 1239–1260.

Bodmer, M., D. R. Toomey, E. E. Hooft, J. Nábělek, and J. Braunmiller (2015). Seismic anisotropy beneath the Juan de Fuca plate system: Evidence for heterogeneous mantle flow, *Geology* **43,** 1095–1098.

Byrnes, J. S., D. R. Toomey, E. E. E. Hooft, J. Nábělek, and J. Braunmiller (2017). Mantle dynamics beneath the discrete and diffuse plate boundaries of the Juan de Fuca plate: Results from Cascadia Initiative body wave tomography, *Geochem. Geophys. Geosys.* **18,** 2906–2929.

Collins, J. A., D. K. Smith, and J. J. McGuire (2012). Seismicity of the Atlantis Massif detachment fault, 30° N at the Mid-Atlantic Ridge, *Geochem. Geophys. Geosys.* **13,** no. 10, doi: 10.1029/2012GC004210.

Crawford, W. C., and S. C. Webb (2000). Identifying and removing tilt noise from low-frequency (< 0.1 Hz) seafloor vertical seismic data, *Bull. Seismol. Soc. Am.* **90,** 952–963.

Dziak, R. P., C. G. Fox, A. M. Bobbitt, and C. Goldfinger (2001). Bathymetric map of the Gorda plate: Structural and geomorphological processes inferred from multibeam surveys, *Mar. Geophys. Res.* **22,** 235–250.

Eason, D. E., R. A. Dunn, J. P. Canales, and R. A. Sohn (2016). Segment-scale variations in seafloor volcanic and tectonic processes from multibeam sonar imaging, Mid-Atlantic Ridge Rainbow region (35°45′–36°35′N), *Geochem. Geophys. Geosys.* **17,** 3560–3579.

Eilon, Z. C., and G. A. Abers (2017). High seismic attenuation at a mid-ocean ridge reveals the distribution of deep melt, *Sci. Adv.* **3,** no. 5, e1602829.

Forsyth, D. W., D. S. Scheirer, S. C. Webb, L. M. Dorman, J. A. Orcutt, A. J. Harding, D. K. Blackman, J. P. Morgan, R. S. Detrick, Y. Shen, *et al.* (1998). Imaging the deep seismic structure beneath a mid-ocean ridge: The MELT experiment, *Science* **280,** 1215–1218.

Gao, H. (2016). Seismic velocity structure of the Juan de Fuca and Gorda plates revealed by a joint inversion of ambient noise and regional earthquakes, *Geophys. Res. Lett.* **43,** 5194–5201.

Gao, H. (2018). Three-dimensional variations of the slab geometry correlate with earthquake distributions at the Cascadia subduction system, *Nature Comm.* **9,** Article Number 1204.

Gao, H., and Y. Shen (2014). Upper mantle structure of the Cascades from full-wave ambient noise tomography: Evidence for 3D mantle upwelling in the back-arc, *Earth Planet. Sci. Lett.* **390,** 222–233.

Gao, H., and Y. Shen (2015). A preliminary full-wave ambient-noise tomography model spanning from the Juan de Fuca and Gorda spreading centers to the Cascadia volcanic arc, *Seismol. Res. Lett.* **86,** 1253–1260.

Goldfinger, C., S. Galer, J. Beeson, T. Hamilton, B. Black, C. Romsos, J. Patton, C. H. Nelson, R. Hausmann, and A. Morey (2017). The importance of site selection, sediment supply, and hydrodynamics: A case study of submarine paleoseismology on the northern Cascadia margin, Washington, USA, *Mar. Geol.* **384,** 4–46.

Goldfinger, C., L. D. Kulm, L. C. McNeill, and P. Watts (2000). Super-scale failure of the southern Oregon Cascadia margin, *Pure Appl. Geophys.* **157,** 1189–1226.

Gomberg, J. (2018). Cascadia onshore-offshore site response, submarine sediment mobilization, and earthquake recurrence, *J. Geophys. Res.* **123,** 1381–1404.

Hammond, W. C., and D. R. Toomey (2003). Seismic velocity anisotropy and heterogeneity beneath the Mantle Electromagnetic and Tomography Experiment (MELT) region of the East Pacific Rise from analysis of *P* and *S* body waves, *J. Geophys. Res.* **108,** no. B4, doi: 10.1029/2002JB001789.

Harmon, N., D. Forsyth, and S. Webb (2007). Using ambient seismic noise to determine short-period phase velocities and shallow shear velocities in young oceanic lithosphere, *Bull. Seismol. Soc. Am.* **97,** 2009–2023.

Lin, F.-C., M. P. Moschetti, and M. H. Ritzwoller (2008). Surface wave tomography of the western United States from ambient seismic noise: Rayleigh and Love wave phase velocity maps, *Geophys. J. Int.* **173,** 281–298.

Lynner, C., and R. W. Porritt (2017). Crustal structure across the eastern North American margin from ambient noise tomography, *Geophys. Res. Lett.* **44,** 6651–6657.

Müller, R. D., M. Sdrolias, C. Gaina, and W. R. Roest (2008). Age, spreading rates, and spreading asymmetry of the world's ocean crust, *Geochem. Geophys. Geosys.* **9,** no. 4, doi: 10.1029/2007GC001743.

Paulatto, M., J. P. Canales, R. A. Dunn, and R. A. Sohn (2015). Heterogeneous and asymmetric crustal accretion: New constraints from multibeam bathymetry and potential field data from the Rainbow area of the Mid-Atlantic Ridge (36° 15′N), *Geochem. Geophys. Geosys.* **16,** 2994–3014.

Rathnayaka, S., and H. Y. Gao (2017). Crustal-scale seismic structure from trench to forearc in the Cascadia subduction zone, *J. Geophys. Res.* **122,** 7311–7328.

Savage, B., B. M. Covellone, and Y. Shen (2017). Wave speed structure of the eastern North American margin, *Earth Planet. Sci. Lett.* **459,** 394–405.

Schulte-Pelkum, V., P. S. Earle, and F. L. Vernon (2004). Strong directivity of ocean-generated seismic noise, *Geochem. Geophys. Geosys.* **5,** no. 3, doi: 10.1029/2003GC000520.

Shapiro, N. M., M. Campillo, L. Stehly, and M. H. Ritzwoller (2005). High-resolution surface-wave tomography from ambient seismic noise, *Science* **307,** 1615–1618.

Shen, W. S., and M. H. Ritzwoller (2016). Crustal and uppermost mantle structure beneath the United States, *J. Geophys. Res.* **121,** 4306–4342.

Shen, Y., Y. Ren, H. Y. Gao, and B. Savage (2012). An improved method to extract very-broadband empirical Green's functions from ambient seismic noise, *Bull. Seismol. Soc. Am.* **102,** 1872–1877.

Smith, S. W., J. S. Knapp, and R. C. Mcpherson (1993). Seismicity of the Gorda plate, structure of the continental-margin, and an eastward jump of the Mendocino Triple Junction, *J. Geophys. Res.* **98,** 8153–8171.

Sumy, D. F., J. A. Lodewyk, R. L. Woodward, and B. Evers (2015). Ocean-bottom seismograph performance during the Cascadia Initiative, *Seismol. Res. Lett.* **86,** 1238–1246.

Tian, Y., and M. H. Ritzwoller (2015). Directionality of ambient noise on the Juan de Fuca plate: Implications for source locations of the primary and secondary microseisms, *Geophys. J. Int.* **201,** 429–443.

Tian, Y., and M. H. Ritzwoller (2017). Improving ambient noise cross-correlations in the noisy ocean bottom environment of the Juan de Fuca plate, *Geophys. J. Int.* **210,** 1787–1805.

Tian, Y., W. S. Shen, and M. H. Ritzwoller (2013). Crustal and uppermost mantle shear velocity structure adjacent to the Juan de Fuca ridge from ambient seismic noise, *Geochem. Geophys. Geosys.* **14,** 3221–3233.

Toomey, D. R., R. M. Allen, A. H. Barclay, S. W. Bell, P. D. Bromirski, R. L. Carlson, X. W. Chen, J. A. Collins, R. P. Dziak, B. Evers, *et al.* (2014). The Cascadia Initiative: A sea change in seismological studies of subduction zones, *Oceanography* **27,** 138–150.

VanderBeek, B. P., and D. R. Toomey (2017). Shallow mantle anisotropy beneath the Juan de Fuca plate, *Geophys. Res. Lett.* **44,** 11,382–11,389.

Velasco, A. A., C. J. Ammon, and T. Lay (1994). Recent large earthquakes near Cape Mendocino and in the Gorda plate—Broad-band source time functions, fault orientations, and rupture complexities, *J. Geophys. Res.* **99,** 711–728.

Webb, S. C. (1998). Broadband seismology and noise under the ocean, *Rev. Geophys.* **36,** 105–142.

Wei, S. S., D. A. Wiens, Y. Zha, T. Plank, S. C. Webb, D. K. Blackman, R. A. Dunn, and J. A. Conder (2015). Seismic evidence of effects of water on melt transport in the Lau back-arc mantle, *Nature* **518,** 395–398.

Wilson, D. S. (1989). Deformation of the so-called Gorda plate, *J. Geophys. Res.* **94,** 3065–3075.

Wong, I. G. (2005). Low potential for large intraslab earthquakes in the central Cascadia subduction zone, *Bull. Seismol. Soc. Am.* **95,** 1880–1902.

Yang, Y. J., and M. H. Ritzwoller (2008). Characteristics of ambient seismic noise as a source for surface wave tomography, *Geochem. Geophys. Geosys.* **9,** no. 2, doi: 10.1029/2007GC001814.

Yao, H. J., P. Gouédard, J. A. Collins, J. J. McGuire, and R. D. van der Hilst (2011). Structure of young East Pacific Rise lithosphere from ambient noise correlation analysis of fundamental- and higher-mode Scholte-Rayleigh waves, *C. R. Geosci.* **343,** 571–583.

Zha, Y., and S. C. Webb (2016). Crustal shear velocity structure in the Southern Lau basin constrained by seafloor compliance, *J. Geophys. Res.* **121,** 3220–3237.

Zha, Y., S. C. Webb, S. S. Wei, D. A. Wiens, D. K. Blackman, W. Menke, R. A. Dunn, and J. A. Conder (2014). Seismological imaging of ridge-arc interaction beneath the Eastern Lau Spreading Center from OBS ambient noise tomography, *Earth Planet. Sci. Lett.* **408,** 194–206.

Zhang, Z. (2010). Full-wave tomography: Method and application to the south-east Tibetan Plateau, *Ph.D. Dissertation*, University of Rhode Island, Kingston, Rhode Island, 122 pp.

Xiaotao Yang
Haiying Gao
Sampath Rathnayaka
Cong Li
Department of Geosciences
University of Massachusetts Amherst
233 Morrill Science Center
627 North Pleasant Street
Amherst, Massachusetts 01003 U.S.A.
xiaotaoyang@geo.umass.edu

Published Online 3 January 2019